JACS
JOURNAL OF THE AMERICAN CHEMICAL SOCIETY
Article
Cite This: J. Am. Chem. Soc. 2018, 140, 9882−9890
pubs.acs.org/JACS

# Dynamically Disordered Lattice in a Layered Pb-I-SCN Perovskite Thin Film Probed by Two-Dimensional Infrared Spectroscopy

Jun Nishida,[†,§] John P. Breen,[§] Kurt P. Lindquist, Daiki Umeyama,[‡] Hemamala I. Karunadasa, and Michael D. Fayer*

Department of Chemistry, Stanford University, Stanford, California 94305, United States

Supporting Information

**ABSTRACT:** The dynamically flexible lattices in lead halide perovskites may play important roles in extending carrier recombination lifetime in 3D perovskite solar-cell absorbers and in exciton self-trapping in 2D perovskite white-light phosphors. Two-dimensional infrared (2D IR) spectroscopy was applied to study a recently reported Pb-I-SCN layered perovskite. The Pb-I-SCN perovskite was spin-coated on a $SiO_2$ surface as a thin film, with a thickness of ∼100 nm, where the $S^{12}CN^-$ anions were isotopically diluted with the ratio of $S^{12}CN$:$S^{13}CN$ = 5:95 to avoid vibrational coupling and excitation transfer between adjacent $SCN^-$ anions. The $^{12}CN$ stretch mode of the minor $S^{12}CN^-$ component was the principal vibrational probe that reported on the structural evolution through 2D IR spectroscopy. Spectral diffusion was observed with a time constant of 4.1 ± 0.3 ps. Spectral diffusion arises from small structural changes that result in sampling of frequencies within the distribution of frequencies comprising the inhomogeneously broadened infrared absorption band. These transitions among discrete local structures are distinct from oscillatory phonon motions of the lattice. To accurately evaluate the structural dynamics through measurement of spectral diffusion, the vibrational coupling between adjacent $SCN^-$ anions had to be carefully treated. Although the inorganic layers of typical 2D perovskites are structurally isolated from each other, the 2D IR data demonstrated that the layers of the Pb-I-SCN perovskite are vibrationally coupled. When both $S^{12}CN^-$ and $S^{13}CN^-$ were pumped simultaneously, cross-peaks between $S^{12}CN$ and $S^{13}CN$ vibrations and an oscillating 2D band shape of the $S^{12}CN^-$ vibration were observed. Both observables demonstrate vibrational coupling between the closest $SCN^-$ anions, which reside in different inorganic layers. The thin films and the isotopic dilution produced exceedingly small vibrational echo signal fields; measurements were made possible using the near-Brewster's angle reflection pump−probe geometry.

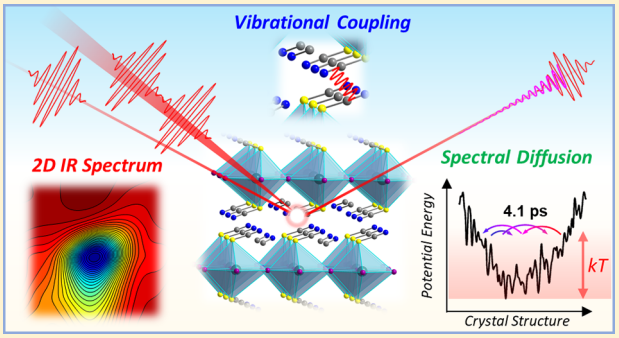


## 1. INTRODUCTION

Three-dimensional (3D) lead halide hybrid perovskites have attracted a great deal of recent interest for their applications in solar cells.[1−3] The low cost for processing perovskite-based solar cells is particularly attractive, rendering them promising candidates for replacing silicon-based solar cells. While the stability and performance lifetime of large-area cells must be improved for practical applications,[4,5] the efficiencies of the perovskite-based solar cells have already surpassed 20%.[6,7] Furthermore, the two-dimensional (2D) analogues within the lead halide perovskite family have been studied as green/blue phosphors since the 1990s,[8] with more recent work showing white-light emission.[9]

Several studies have probed the ground-state and electronic excited-state lattice dynamics in halide perovskites.[10−13] The outstanding photovoltaic performance of 3D lead halide perovskites has been attributed, at least in part, to their dynamical flexibility. In 3D Pb-I perovskites, optical excitation generates free electrons and holes as carriers.[14−18] Some studies have suggested that the local lattice surrounding these carriers reconfigures to stabilize the carriers and impede recombination, leading to the unusually long carrier diffusion length in these absorbers despite their direct bandgap. The result is high power conversion yields.[12,13,19,20] Layered or 2D perovskites have a much higher exciton (excited electron−hole pair) binding energy than their 3D congeners, owing to the spatial confinement of the inorganic layers and the low dielectric constant of the organic layers.[21] More pronounced excited-state lattice distortions have been proposed as the origin of white-light emission upon UV excitation from 2D Pb-Br and Pb-Cl perovskites.[9] In these 2D perovskites, optical excitation generates excitons that are thought to self-trap through transient lattice distortions, leading to a very broad and Stokes-shifted emission.[22] Although self-trapping can occur in static or flexible lattices, dynamic lattice fluctuations may allow the exciton to sample a more extensive landscape of energy minima and promote exciton localization and stabilization through lattice distortions.

Received: April 8, 2018
Published: July 19, 2018






DOI: 10.1021/jacs.8b03787
J. Am. Chem. Soc. 2018, 140, 9882−9890

The examples given above suggest dynamically flexible lattices in 2D and 3D halide perovskites. Recently there have been a few reports that directly observe the thermal fluctuations of the lattices in single crystals of 3D perovskites at room temperature. Yaffe et al. described broad low-frequency Raman spectra centered at zero-frequency in single crystals of $(CH_3NH_3)PbBr_3$ and $CsPbBr_3$,[11] indicating that the lattice constantly undergoes thermal fluctuations. Miyata et al. observed the structural relaxation of the same 3D perovskites in the time-domain using time-resolved optical Kerr effect (TR-OKE) spectroscopy, and the relaxations were interpreted in the context of "large polaron" formation.[23] The ability of the perovskite lattices to reconfigure on a fast time scale is believed to be important for stabilizing photogenerated carriers.[19]

Here, we show that a thin film of a 2D perovskite, $(CH_3NH_3)_2[PbI_2(SCN)_2]$ (Figure 1A), exhibits fast structural changes using two-dimensional infrared (2D IR) spectroscopy. 2D IR spectroscopy has been successful in characterizing the structural dynamics of a variety of flexible materials.[24−30] While 2D NMR spectroscopy (such as EXSY) characterizes dynamics occurring in microseconds or slower time scales, 2D IR spectroscopy can directly observe the structural dynamics occurring in sub-picosecond to nanosecond time scales. The long time limit is determined by the vibrational lifetime of the mode used as the vibrational probe. In the experiments presented here, the lifetime limits the measurements to a few tens of picoseconds. 2D IR spectroscopy monitors the temporal evolution of a molecular vibrational frequency within an inhomogeneously broadened vibrational spectrum. As the vibrational frequency is sensitive to the environment interacting with a molecule, fluctuations in structure lead to changes in the probe's vibrational frequency.[31−33] Therefore, a measurement of the time dependence of the vibrational frequency reports on the time-scale of the interconversion among the different local structures that give rise to the inhomogeneously broadened absorption spectrum of the vibration under study.

Figure 1A shows the crystal structure of the $(CH_3NH_3)_2[PbI_2(SCN)_2]$ layered perovskite.[34−36] This perovskite is referred to as the Pb-I-SCN perovskite hereafter. The Pb-I-SCN perovskite has a distinct two-dimensional layered structure, with corner-sharing octahedra containing central $Pb^{2+}$ ions coordinated to bridging iodides and terminal thiocyanates. Small $CH_3NH_3^+$ cations reside close to the anionic inorganic layers, providing charge balance. The lattice is highly compressible with a particularly low ambient-pressure bulk modulus ($K_0$) of 7.6(8) GPa.[35] In contrast, the $K_0$ values of oxide perovskites are greater than 100 GPa.[37] Given the soft nature of the material, we postulated that the lattice may undergo fast structural fluctuations. Even though the organic cations are fixed in the lattice, our measurements reveal that the lattice structure undergoes diffusive thermal fluctuations, which were observed as a decay in the time correlation of the CN vibrational frequency (spectral diffusion). Such ultrafast dynamical flexibility found in the 2D perovskite structure can be important for the immediate stabilization of the photogenerated excitons. The diffusive fluctuations of local structures are distinct from phonons, the oscillatory motions of structure about the average structural configuration.

The performance of the perovskite-based devices is well-known to be strongly dependent on the morphology of the crystals within the devices.[38] It is thus useful to study perovskite structural dynamics in the morphology relevant to the devices, i.e., thin films. A challenge of applying 2D IR spectroscopy to perovskite films with the thickness of ∼100 nm is the weak signal produced by the small number of vibrational chromophores in the thin films. In the study presented here, this problem is compounded by isotopic dilution of the SCN chromophores, which is necessary to extract the dynamical information of interest. Using standard methods, the observed signal level is orders of magnitude smaller than bulk solution samples commonly studied with 2D IR spectroscopy. The employment of BOXCARS geometry with an external local oscillator[32] alleviates this problem to a significant extent, but the slow data acquisition rate and phase ambiguity hinder the detailed observations of the structural fluctuations.

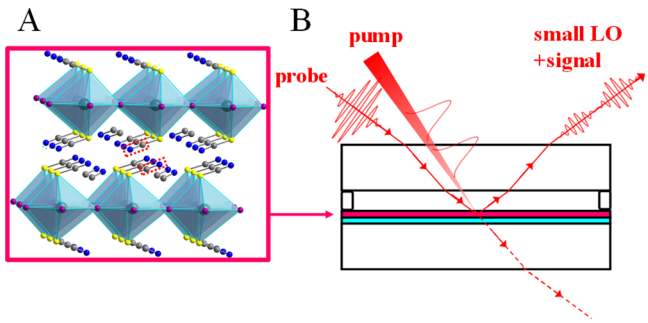


**Figure 1.** (A) The structure of the 2D perovskite $(CH_3NH_3)_2PbI_2(SCN)_2$ (abbreviated as Pb-I-SCN). Color code: turquoise, Pb; purple, I; yellow, S; gray, C; blue, N; H atoms omitted for clarity. The CN stretching modes of two adjacent SCN anions (indicated by dotted red lines) are coupled by transition dipole−transition dipole interactions. (B) The sample configuration drawn together with incident and output laser pulses for reflection enhanced 2D IR spectroscopy. The sample film (red layer) was spin-coated onto a 100 nm $SiO_2$ layer, which was deposited on a 3 mm $CaF_2$ window. The sample was prepared in a $N_2$-filled glovebox, and an O-ring and another $CaF_2$ window were placed on the top to isolate the sample film from atmospheric moisture. Two pump pulses and one probe pulse were sent through the sample film, where the incident angle of the probe pulse, 53°, was set close to the Brewster's angle (54.5°). The small probe reflection as the local oscillator, together with the signal field, was sent to a spectrograph and detected by a 32-element HgCdTe array detector.

A new approach, 2D IR spectroscopy with near-Brewster's angle reflection pump−probe geometry, has proven useful for the study of molecular monolayers.[39] This geometry essentially combines (1) phase stability achieved by acousto-optic modulator (AOM) pulse shaping system and self-heterodyne between a local oscillator (LO) and a vibrational echo signal,[40,41] and (2) reduction of the LO amplitude relative to the vibrational echo signal amplitude resulting in high signal-to-background ratio. These two important features yield high quality two-dimensional band shapes with fast data acquisition rates even with samples that are thin films or even monolayers.[39,42]

2D IR spectroscopy requires vibrational probes in the system of interest, and the CN stretching mode of the $SCN^-$ anions was used as the vibrational probe.[43] As seen in Figure 1A, an $SCN^-$ has another $SCN^-$ from an adjacent sheet in close proximity, which, as shown below, results in vibrational couplings and vibrational excitation transfer. These two factors can complicate the interpretation of the observed two-dimensional band shapes. To address these issues, we isotopically diluted the SCN anions[44] ($S^{12}CN$:$S^{13}CN$ = 5:95)


DOI: 10.1021/jacs.8b03787
J. Am. Chem. Soc. 2018, 140, 9882−9890

and controlled the spectral profile of the pump pulses (pulses 1 and 2 in the three pulse 2D IR pulse sequence).[45]

This paper is organized in the following manner. In section 2, the sample preparation and the configuration of the laser system are summarized. In section 3, we discuss the infrared absorption spectra of the prepared perovskite thin films, the pump−probe signal, and two-dimensional band shapes. A significant enhancement in the signal-to-background ratio in the reflection geometry and a contribution from dispersive line shape were both confirmed for the thin film sample, as predicted in a previous publication.[39] In section 4, the 2D IR spectra acquired with the full pump spectral profile are discussed. The observed cross peaks between $^{12}$CN and $^{13}$CN stretching modes and the characteristic oscillation of the 2D band shape of the $^{12}$CN mode confirm the vibrational coupling between the adjacent anions. The transition dipole−transition dipole coupling mechanism was demonstrated by a calculation based on the transition dipole amplitude and the distance and angle between the anions obtained from the crystal structure.[34] Then in section 5, the evolution of the 2D band shape observed by pumping the $^{12}$CN mode but not the $^{13}$CN mode is discussed. The band shape observed in this manner is free from influences of vibrational coupling or excitation transfer and reflects the structural evolution of the system.

## 2. EXPERIMENTAL PROCEDURES

**Isotopically Diluted Pb-I-SCN Perovskite Thin-Film Preparation.** The Pb-I-SCN perovskite was spin-coated on a 100 nm $SiO_2$ film deposited on a 3 mm thick $CaF_2$ substrate (1-in. diameter) by plasma-enhanced chemical vapor deposition (UCSB Nanofabrication Facility).[46] The $SiO_2/CaF_2$ wafer transmits incident infrared pulses and was useful for the optical alignment as briefly discussed below.

The Pb-I-SCN perovskite was prepared based on a previously published procedure[35] with some modifications. Potassium thiocyanate (KS$^{12}$CN and KS$^{13}$CN), lead(II) nitrate ($Pb(NO_3)_2$), methylammonium iodide ($[CH_3NH_3]I$), and tetrahydrofuran (THF) were purchased from Sigma-Aldrich and used without further purification. In the entire processes below, the exposure to light was minimized by either wrapping the solution/solid containers with aluminum foil or turning off lights. 4.1 mg of KS$^{12}$CN and 86.5 mg of KS$^{13}$CN were dissolved in 840 $\mu$L of water. 150.9 mg of $Pb(NO_3)_2$ was separately dissolved in 1.5 mL of water. The $Pb(NO_3)_2$ solution was placed in an ice bath while stirring, and the KSCN solution was injected. The solution was stirred for 30 min, and a colorless powder of $Pb(SCN)_2$ with S$^{12}$CN:S$^{13}$CN = 5:95 was formed. The $Pb(SCN)_2$ was filtered by suction filtration and dried overnight.

20.3 mg of the isotopically mixed $Pb(SCN)_2$ and 20.3 mg of $(CH_3NH_3)I$ were placed in a vial, and 1.6 mL of THF was added. The solution was sonicated for 10 min to dissolve both the solids to yield a yellow solution. The solution was filtered with an inorganic membrane filter (0.1 $\mu$m) and used for the spin-coating.

The precursor solution and the $SiO_2/CaF_2$ substrate were transferred to a nitrogen glovebox. 200 $\mu$L of the solution was loaded on the substrate and spin-coated using a home-built spin-coater at 3000 rpm for 30 s. A scarlet film of the Pb-I-SCN layered perovskite was formed on the substrate. As noted previously, the Pb-I-SCN film decomposes in ambient humidity.[35] To avoid exposure to atmospheric humidity, the substrate was spin-coated in and kept in a nitrogen glovebox. The sample was sealed in the sample cell (sample substrate, $CaF_2$ window and 1 mm-thick O-ring, Figure 1B).

The powder X-ray diffraction (PXRD) pattern, UV−Vis absorption spectrum, and photoluminescence spectrum of the Pb-I-SCN spin-coated films were reported in a previous publication.[35] These sample characterizations are presented and discussed in the Supporting Information. The final measurements of pump-probe and 2D IR were conducted on samples that were prepared both for the PXRD measurements and the IR experiments in an identical manner. Due to the sensitivity of the sample to the humidity, we could not characterize the sample thickness using a standard technique such as atomic force microscopy (AFM). Instead, we determined the thickness the films using the absorption of CN stretch in transmission FT-IR spectra, which shows the thickness of the films to be in the range of 50 to 100 nm. See Supporting Information for details.

**Ultrafast Infrared Laser System and the Near-Brewster's Angle Reflection Geometry.** The laser system and the implementation of near-Brewster's angle reflection pump−probe geometry were described in detail in a previous publication.[39] An infrared pulse (30 $\mu$J, ∼160 fs fwhm, ∼95 cm$^{-1}$ fwhm, centered at 2080 cm$^{-1}$) was split into a pump pulse (92%) and a probe pulse (8%). The pump pulse was sent to a germanium acousto-optic modulator (Ge-AOM) pulse shaping system, both to control the temporal profile of the pump pulses and to filter some of the frequency components as discussed below. The pump pulses were focused into the sample with a $f$ = 15 cm lens, and the probe pulse was focused with a $f$ = 10 cm lens. The probe pulse arrived after the pump pulses with a controlled delay time. Excessive energy of the pump pulses degraded the samples. Therefore, pump intensity at focus was thus attenuated to ∼30 mJ/cm$^2$ to avoid sample damage.

The sample (Figure 1B) was placed so that the incident angle of the probe pulse was 53°, which is close to Brewster's angle for $CaF_2$, 54.5°. The Pb-I-SCN sample layer was placed at the focus of the pump/probe pulses. The reflected probe beam from the surface containing the Pb-I-SCN film (the third surface from the top as shown in Figure 1B) was then selected and collimated with another $f$ = 10 cm lens, sent to a spectrograph, and detected by an HgCdTe array detector. Note that there are four reflections of the probe pulse caused by the four surfaces. Though these reflections are tightly spaced right after the sample, the collimating lens steers these reflections differently. Consequently, all the reflections were separated by >2 cm in front of the monochromator. Therefore, the influence of the other reflections on the detected signal was eliminated.

**Spectral Filtering of Pump Pulse.** The AOM pulse shaper can remove some of the frequency components of the incident pump pulses. The details are outlined in previous publications.[45,47] When we addressed the coupling between $^{12}$CN and $^{13}$CN vibrations in adjacent anions, we employed pump pulses with the full spectrum. We will call this pumping scheme "full pump" in the following discussions. On the other hand, the coupling or heating induced by pumping the S$^{13}$CN anions, the 95% majority component, hinders the extraction of the dynamical information stored in the observed pump−probe or 2D spectra. To circumvent the problem, the pump spectrum was often modified by removing the spectral region where the $^{13}$CN vibration is located (2015−2055 cm$^{-1}$).[45,48] The spectral shaping with a Hann window was employed to avoid the effects of hard edges of the pump spectrum. This pumping scheme will be called the "(spectrally) filtered pump" (see Figure 2A).

Note that by filtering the pump spectral profile, the pump pulse is slightly broadened in time. Careful attention must be paid to avoid potential contributions from non-resonant signals or signals arising from unwanted time-ordered pathways such as perturbed free-induction decays.[49] Based on the pump−probe SHG cross-correlation we acquired with the spectrally filtered pump pulse,[45] we determined that the pump−probe or 2D IR signals acquired after $T_w$ = 2 ps are free from these potential artifacts. Therefore, the pump−probe signals (Figure 2B) and 2D IR band shapes (see Figure 4B, below) acquired with the spectrally filtered pump pulse were analyzed only after $T_w$ = 2 ps.

## 3. INFRARED SPECTROSCOPY ON THE LAYERED PEROVSKITE

**Infrared Absorption Spectroscopy.** The black lines in Figure 2A show a typical infrared absorption spectrum acquired in the standard transmission geometry. Our main focus is the 2080 cm$^{-1}$ band arising from the $^{12}$CN stretch of the minor S$^{12}$CN (5%) anion component in the isotopically diluted layered perovskite. As seen in the inset, this $^{12}$CN band


DOI: 10.1021/jacs.8b03787
J. Am. Chem. Soc. 2018, 140, 9882−9890

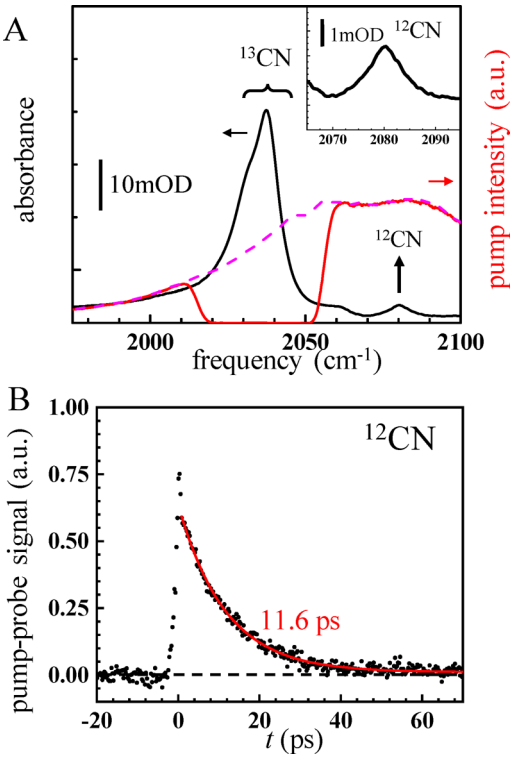


**Figure 2.** (A) Black solid line is the FT-IR absorption spectrum of the isotopically doped Pb-I-SCN film acquired in transmission geometry. While the large band around 2030–2040 cm$^{-1}$ arises from the major S$^{13}$CN$^-$ component, the minor feature at ~2080 cm$^{-1}$ originates from the minor S$^{12}$CN$^-$ anions. Inset shows an expanded view of the $^{12}$CN absorption band. While the $^{13}$CN vibration clearly exhibits a shoulder at ~2030 cm$^{-1}$, the shoulder is absent in the $^{12}$CN spectrum. This is one of the signatures of the vibrational coupling between adjacent SCN$^-$ anions. Red solid line is the spectrum of the "filtered" pump pulse in this region. The pump spectrum was modified by the AOM to avoid excitation of the $^{13}$CN mode. In contrast, in the full pump spectrum experiments, the $^{13}$CN mode is also pumped, as indicated by the dashed magenta line. (B) Infrared pump–probe signal acquired at the probe frequency of 2080 cm$^{-1}$ with the pump spectrum filtered so that the $^{13}$CN vibration is not excited. The relatively long lifetime, 11.6 ps, provided more than a 20 ps time window over which the structural evolution was monitored with 2D IR spectroscopy. The pump–probe signal decays to zero, demonstrating that there is little sample heating by the laser.

is a single peak. In contrast, the major $^{13}$CN stretch from S$^{13}$CN (95%) clearly consists of two bands, i.e., the major band at ~2037 cm$^{-1}$ and a large shoulder on the red side at ~2030 cm$^{-1}$. Accurate determination of the peak positions was difficult due to the small separation of the two bands.

The two bands in the $^{13}$CN stretch spectrum can be explained by the vibrational coupling between two adjacent S$^{13}$CN anions.[50] Coupling between the CN vibrations of the closely spaced S$^{13}$CN anions leads to a splitting of the absorption band, which is equivalent to the well-known Davydov splitting in the electronic spectroscopy of crystals with two or more molecules in the unit cell. The splitting of the $^{13}$CN vibrational band can be regarded as a vibrational version of Davydov splitting. The splitting is not observed in the S$^{12}$CN band, as S$^{12}$CN is diluted in the structure, and it is not statistically likely that there are two adjacent S$^{12}$CN anions. When an S$^{12}$CN is adjacent to a S$^{13}$CN, the difference in the $^{12}$CN and $^{13}$CN vibrational frequency is large compared to the coupling. The coupling will produce a very small frequency shift of the $^{12}$CN band, but no splitting.[51] Isotopic dilution has been frequently used to eliminate vibrational excitation transfer in the study of dynamics of water (HOD in $H_2O$ or $D_2O$).[27,31]

There are two possible vibrational coupling mechanisms, mechanical coupling and transition dipole–transition dipole coupling.[50,52] Mechanical coupling is a result of the anharmonicity of the vibrational potential. The vibration of one mode must be coupled through chemical bonds to another mode of a molecule. In this case, mechanical coupling can only take place between two adjacent SCN anions that are chemically connected through the Pb atom. However, the mechanical coupling is expected to be very weak as the large mass of Pb effectively isolates the CN vibrations of the two anions. An example of a massive atom decoupling vibrations is the fact that the CN stretch of benzonitrile has a lifetime of 7 ps while the CN of cyanoselenobenzene has a lifetime of 300 ps.[44,53] The heavy selenium effectively decouples the CN stretch from the modes of the benzene, blocking effective pathways for vibrational relaxation.

Transition dipole–transition dipole coupling is through space.[54] The two anions do not have to be on the same molecule. As seen in Figure 1A, there are two adjacent SCN$^-$ anions in different inorganic layers that are not chemically bound but can be coupled because of their proximity, ~4 Å apart (the distance was measured as the distance between the centers of the two adjacent CN bonds).

The transition dipole–transition dipole coupling can be calculated based on the reported crystal structure and the transition dipole moment of the CN stretching mode of the SCN$^-$. Sodium thiocyanate (NaSCN) was dissolved in dimethyl sulfoxide (DMSO), and an infrared absorption spectrum was acquired to determine the transition dipole moment magnitude of the CN stretch ($|\mu_T| = 9.1 \times 10^{-31}$ C·m). The transition dipole–transition dipole coupling constant, $J$, is given by

$$J = \frac{1}{4\pi\varepsilon_0 |\vec{r}|^3}\{\vec{\mu}_1\cdot\vec{\mu}_2 - 3(\vec{\mu}_1\cdot\vec{r})(\vec{\mu}_2\cdot\vec{r})/|\vec{r}|^2\} \quad (1)$$

where $\vec{r}$ is a vector connecting the centers of the two CN bonds, and $\vec{\mu}_1$ and $\vec{\mu}_2$ are the transition dipole moment vectors for the two CN vibrations. We take the transition dipole to be along the CN bond. Based on the crystal structure in Figure 1A, the coupling constant $J$ was estimated to be 4.4 cm$^{-1}$. Because the vibrational frequencies for the two oscillators are identical, the splitting is $2J$.[51] The calculated splitting is thus 8.8 cm$^{-1}$, which is quite close to the observed splitting of ~7 cm$^{-1}$. Note that the transition dipole moment in the perovskite lattice could be weaker than that of SCN$^-$ in solution due to the covalent nature of Pb–SCN bonding, which may account for the slight overestimation of the splitting compared with the experimental value. For example, ethylSCN has a smaller transition dipole than SCN$^-$. Nonetheless, the calculation supports the transition dipole–transition dipole coupling mechanism between SCN$^-$ ligands.

Note that the identical coupling calculation was applied to the second closest SCN$^-$ anion pair, which are ~6 Å apart. The calculation yielded the splitting $2J$ of 4 cm$^{-1}$. This smaller splitting is obscured by the intrinsic absorption bandwidth (8 cm$^{-1}$ fwhm) and was not manifested in either linear or nonlinear spectroscopy experiments.

We observed that the ratio of the absorption amplitudes between the ~2037 cm$^{-1}$ and ~2030 cm$^{-1}$ bands from the


DOI: 10.1021/jacs.8b03787
J. Am. Chem. Soc. 2018, 140, 9882–9890

$S^{13}CN^-$ anions varies from sample to sample. This variance could be explained by different orientations of the crystalline domains in different films. As is the case with most other 2D perovskites, powder X-ray diffraction of the films show preferred orientation, with the inorganic sheets lying parallel to the substrate (with the sheets stacking along the crystallographic *a* axis).[35] However, the crystallites are randomly ordered along the *b* and *c* axes. Note that the eigenstates, the sum and difference of the two coupled vibrational modes, have transition dipole moments that are orthogonal in the crystal. For the measurement of the absorption spectrum, the incident beam was sent almost normal to the surface and therefore the polarization was in the plane of the surface. Depending on the crystal orientations within the plane of the inorganic sheets, the field−dipole interactions for the two modes can be different, which leads to the varying ratios.

**Pump−Probe Spectroscopy: Vibrational Lifetime and Heating Effects.** Figure 2B shows the infrared pump−probe signal acquired at the optical frequency of 2080 $cm^{-1}$ ($^{12}CN$ stretch) with the spectrally filtered pump pulse (see section 2) so that the $^{13}CN$ stretch is not pumped. The polarization for the pump and probe pulses are parallel. As the orientational motions of the SCN anions are strongly restricted due to the rigid Pb-SCN bond, the observed pump−probe signal decay is solely attributed to vibrational relaxation.[55]

There are two important features observed in Figure 2B. First, the decay occurs with the vibrational lifetime of 11.6 ps. This relatively long lifetime of the $^{12}CN$ stretching mode allows the tracking of the evolution of the two-dimensional band shape in 2D IR spectroscopy. Another important point is that the pump−probe signal decays to zero after long enough time, indicating the absence of the significant heating of the sample. This is another advantage of spectrally filtering the pump pulse so that the majority of the anions ($S^{13}CN$) are not pumped. When the pump−probe signal was acquired with a pump pulse with the full spectral profile, a strong heating signal was observed, which complicated the interpretation of data, particularly that of 2D IR spectroscopy.[31]

**Two-Dimensional Infrared Spectroscopy: Dispersive Line Shape.** Figure 4A discussed in section 5 shows 2D IR spectra acquired with the spectrally filtered pump pulse. Along the $\omega_m$ axis, dispersive line shapes contribute to the observed 2D spectra, in addition to absorptive line shapes. The phases of the absorptive and dispersive line shapes are exactly in agreement with the predictions in a previous report.[39] The mechanism that gives rise to the dispersive line shape contribution was discussed there in detail as well. Briefly, the signal field emitted inside the film is phase-shifted from the signal from the very top of the film due to the additional optical path, which results in the emergence of the dispersive line shape.[39]

While the observed 2D band is not purely absorptive, it was demonstrated previously that the center line slope (CLS) of the band shape is preserved regardless of the contribution from the dispersive line shape.[39] The CLS($T_w$) is the normalized frequency−frequency correlation function (FFCF), which reflects the structural dynamics of the medium that give rise to spectral diffusion.[33,56] The FFCF decays in time as structural fluctuations occur and randomize the vibrational frequency within the inhomogeneously broadened absorption band; therefore, FFCF is a good measure for the structural dynamics occurring in the film.

In the following two sections, 2D IR spectra acquired with the pump pulses with the full (section 4) and filtered (section 5) spectral profiles are presented to address vibrational coupling and structural dynamics of the perovskite structures, respectively.

## 4. VIBRATIONAL COUPLING REVEALED BY 2D IR SPECTROSCOPY

**Off-Diagonal Cross-Peak.** Figure 3A shows the 2D IR spectrum acquired with the full pump spectrum at $T_w$ = 1 ps. The diagonal peak observed in the 2030−2050 $cm^{-1}$ region of Figure 3A reveals major and minor features arising from the two absorption peaks discussed in section 3, namely the ∼2030 $cm^{-1}$ peak and the ∼2037 $cm^{-1}$ peak. In the 2D IR spectrum, the coupling of the two vibrations produces off-diagonal cross-peaks between the two vibrations. However, the amplitude of the 2030 $cm^{-1}$ peak is so small compared with the 2037 $cm^{-1}$

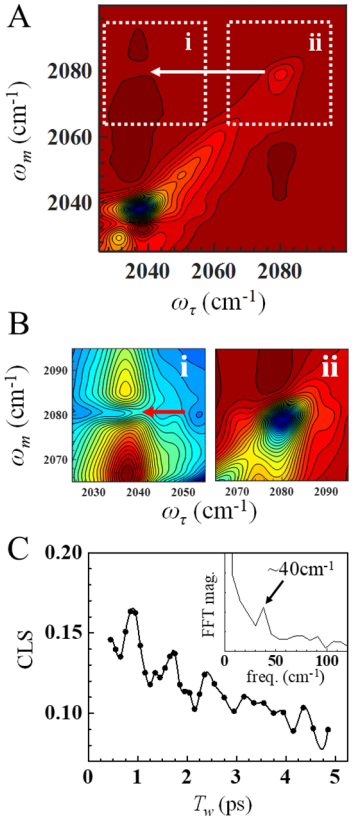


**Figure 3.** (A) 2D IR spectrum of isotopically doped Pb-I-SCN perovskite acquired with the full pump spectrum, which pumps both $^{12}CN$ and $^{13}CN$ vibrations. The spectrum was acquired at $T_w$ = 1 ps. (B) Expanded views of regions (i) and (ii) in the full spectrum shown in panel A. Region (i), which corresponds to the off-diagonal region between $^{12}CN$ and $^{13}CN$ vibrations, shows that the positive dispersive signal from the $^{13}CN$ vibration is eaten out by a negative cross peak between the two vibrations (red arrow). Region (ii) shows the diagonal peak for the $^{12}CN$ vibration, which can be analyzed with the CLS method to further reveal the vibrational coupling between $^{12}CN$ and $^{13}CN$ vibrations. (C) Temporal evolution of the CLS for the $^{12}CN$ diagonal peak shown in B-(ii). The black dots show the raw data, which exhibit an oscillatory feature. The solid line is a cubic spline to the observed data with 10 fs increments. Inset shows the fast Fourier transform magnitude of the splined data. A peak is observed at ∼40 $cm^{-1}$, which corresponds well to the splitting between $^{12}CN$ and $^{13}CN$ vibrations.



DOI: 10.1021/jacs.8b03787
J. Am. Chem. Soc. 2018, 140, 9882−9890

peak that the observation of the cross-peaks is difficult. The contribution of the dispersive line shape further complicates the identification of the cross peaks.

To address the coupling between two adjacent vibrations, it is easier in this case to observe the cross-peaks between $^{12}$CN and $^{13}$CN vibrations, which are well separated in frequency. Note that while the adjacent $^{12}$CN and $^{13}$CN vibrations do not induce a splitting because of the large separation in the vibrational frequencies,[51] they are still coupled through the transition dipole−transition dipole interaction, and cross-peaks should be observed in the 2D spectra.

Two important subparts of Figure 3A are expanded in Figure 3B providing a path for analysis of the vibrational coupling. The cross-peak is most clearly visible in panel (i) in Figure 3A,B. The positive (red) feature arises from the dispersive line shape of the major $^{13}$CN vibration. Clearly, the positive feature is reduced right at $\omega_m$ = 2080 cm$^{-1}$, where the $^{12}$CN vibration is located (see arrow). The negative cross peak eats a hole in the positive going peak. This feature shows the existence of the negative-going cross-peak between the $^{13}$CN vibration ($\omega_\tau$ = 2037 cm$^{-1}$) and the $^{12}$CN vibration ($\omega_m$ = 2080 cm$^{-1}$). The observation of the off-diagonal cross-peak verifies that the two adjacent CN vibrations are coupled. However, because of the complexity of the spectrum, it is easier to see the effect of coupling in the time domain as discussed below.

**Center Line Slope Oscillations.** As confirmation of the coupling of the adjacent CN vibrations, we investigated the waiting time ($T_w$) dependence of the CLS of the diagonal peak arising from the $^{12}$CN vibration. The peak corresponds to panel (ii) in Figure 3A,B. The 2D IR spectra were again acquired with full spectrum pumping.

Figure 3C shows the $T_w$-dependence of the CLS. The CLS clearly oscillates in time (compare to Figure 4B). The inset in Figure 3C shows the Fourier transform magnitude spectrum of the oscillation. The oscillation frequency of ∼40 cm$^{-1}$ can be readily identified, which corresponds very well to the separation between $^{12}$CN and $^{13}$CN vibrations.

This oscillation in CLS is another signature of the vibrational coupling between the two vibrational modes. The mechanism of the CLS oscillation was discussed in detail in a previous publication.[45] Briefly, two interactions from the pump pulses each excite both the $^{12}$CN and $^{13}$CN vibrations, forming a coherence between the two vibrations during the waiting ($T_w$) period. This pathway introduces a non-rephasing signal with amplitude and phase oscillating with time, leading to the oscillation in CLS.

Overall, the cross-peak and the oscillations in the CLS observed with 2D IR spectroscopy verify that the adjacent CN vibrations are coupled, and the coupling leads to the splitting of the $^{13}$CN vibration absorption band. The two peaks originating from the splitting were indeed observed in the absorption spectrum (Figure 2A), and are well explained by transition dipole−transition dipole coupling (section 3). When a pure S$^{12}$CN sample was prepared, the absorption band was also composed of two peaks with the same splitting.

Though the oscillation is useful to identify the vibrational coupling, it hinders the accurate assessment of the structural dynamics through the CLS decay. The filtered pumping scheme eliminates the oscillations and yields the 2D band shape evolution caused purely by structural dynamics, as discussed in section 5.

## 5. STRUCTURAL FLUCTUATION OF THE LAYERED PEROVSKITE

To address the structural dynamics occurring in the Pb-I-SCN layered perovskite without interference from vibrational coupling, the spectrally filtered pumping scheme was employed to acquire 2D IR spectra for the $^{12}$CN vibration. Figure 4A shows two 2D IR spectra acquired at $T_w$ = 2 ps and $T_w$ = 20 ps. A subtle change in the 2D band shape can be observed between the two spectra. The changes in the 2D spectra shapes with $T_w$ are quantified with the CLS method. The slopes of the dashed white lines in Figure 4A are the CLS. As $T_w$ increases the slope becomes smaller, approaching zero at long times.

2D IR spectra were acquired for the various waiting times between 2 and 25 ps, and the CLS values were calculated around the main negative-going feature. The series of 2D IR spectra were acquired from three independent samples, and they yielded very similar CLS decays. The CLS decays were weighted based on the number of scans and averaged to yield an averaged CLS decay with reasonable signal-to-noise ratio as shown in Figure 4B. The CLS decay in Figure 4B was fit well by a single exponential plus offset, and yielded the time constant of 4.1 ± 0.3 ps with a 0.09 offset. Note that the total decay amplitude is quite small (∼0.1). Again, the CLS decay is the normalized FFCF decay, independent of the contribution from the dispersive line shape. The experiments shown in Figure 4B were taken on samples with 5% $^{12}$C and 95% $^{13}$C SCN. To confirm the negligible coupling and excitation transfer between the low concentration of pairs of $^{12}$C SCNs, the experiments were repeated with samples with 1% $^{12}$C and 99% $^{13}$C SCN. The results were identical.

When the CLS decay is extrapolated to $T_w$ = 0 ps based on the fit, it yields the value of ∼0.2. The maximum possible value is 1. The difference between the observed $T_w$ = 0 value and 1 is a measure of the homogeneous line width. This small value of the CLS at $T_w$ = 0 indicates that the $^{12}$CN absorption band is substantially homogeneously broadened. Analyzing the data quantitatively, the homogeneous line width was determined to be 6 cm$^{-1}$ out of the total 8 cm$^{-1}$ full width at half-maximum (fwhm) of the absorption band. The total line width is the convolution of the homogeneous component with the inhomogeneously broadened component. The inhomogeneous width reflects structural disorder in the crystal. Some of this disorder is not static but rather dynamic, unlike static disorder caused by crystal lattice strains or defects. Such dynamical disorder is observed as the 4.1 ps spectral diffusion, which originates from fast sampling of different structures. Out of the 8 cm$^{-1}$ fwhm line width, the 3.5 cm$^{-1}$ fwhm inhomogeneous line width component is sampled by structural fluctuations. It is important to recognize that spectral diffusion is not caused by lattice phonons. Rather, the observed spectral diffusion is caused by transitions from one local lattice configuration to another via transitions from one small potential energy minimum to another on the rough energy landscape shown schematically as the black curve in Figure 4C. Different structures give rise to different CN vibrational frequencies, e.g., due to slightly different distance between $SCN^-$ anions and $CH_3NH_3^+$ cations. Thermally driven transitions from one local minimum to another, as indicated in Figure 4C, result in frequency changes, which were detected as the spectral diffusion with the time constant of 4.1 ps.

The observation here of the spectral diffusion of the CN vibrational mode of the $SCN^-$ anion demonstrates the $SCN^-$



DOI: 10.1021/jacs.8b03787
J. Am. Chem. Soc. 2018, 140, 9882−9890

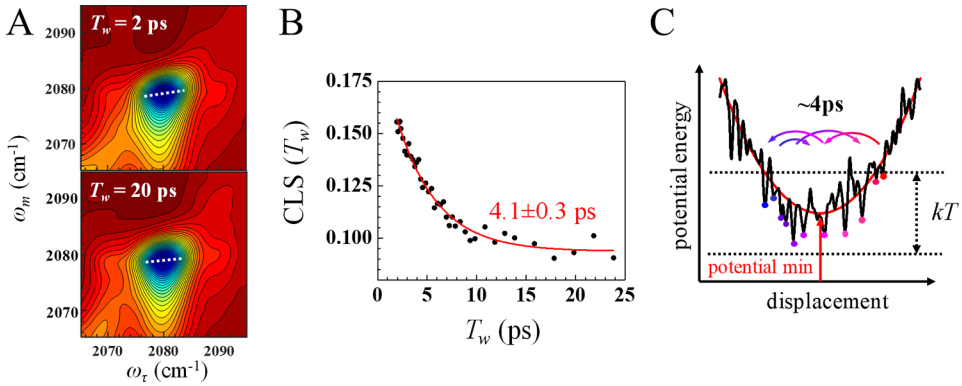


**Figure 4.** (A) 2D IR spectra of the $^{12}$CN vibration acquired with the spectrally filtered pump pulse so that the $^{13}$CN vibration is not pumped. The changes in the CLS (the slope of the white dotted line) with time give the normalized FFCF. (B) CLS decay acquired from a series of time-dependent 2D IR spectra. The spectra from three different samples were averaged. The decay time constant, 4.1 ± 0.3 ps, arises from the structural fluctuations of the perovskite structure. (C) Schematic of the potential energy surface. The red curve is the potential energy of the periodic lattice. Oscillatory motions about the minimum are the lattice phonons. The observation of the inhomogeneously broadened absorption band and the spectral diffusion shows that there is a rough energy landscape with many small potential minima (black curve). Each minimum is a distinct local structure. A particular minimum will be associated with a frequency in the inhomogeneously broadened absorption band. Spectral diffusion is associated with transitions (colored arrows) from one minimum to another.

anion is part of a dynamical lattice structure in the Pb-I-SCN layered perovskite. The spectral diffusion decay shows that the layered perovskite structure is constantly undergoing fast structural changes with a time constant of 4.1 ± 0.3 ps. The dynamical disorder in the 2D perovskite may play a role in stabilizing excitons soon after they are generated before recombination can take place.

As shown by the small offset in the CLS (0.09), a small fraction (2.5 cm$^{-1}$ fwhm) of the vibrational absorption band (8 cm$^{-1}$ fwhm band) is not sampled by the structural fluctuations discussed above and appears as static inhomogeneity over the observable time window. As the observable time range is limited by the vibrational lifetime of the SCN (~11 ps), we cannot exclude the possibility that much slower (>100 ps) local structural fluctuations sample this inhomogeneity, leading to complete spectral diffusion. However, considering that the film is polycrystalline and contains various crystals with different sizes and strains, it is possible that the small residual inhomogeneity arises from the static inhomogeneity due to strains, defects and grain boundaries.

## 6. CONCLUDING REMARKS

Two-dimensional infrared (2D IR) spectroscopy was applied to a thin film of the Pb-I-SCN layered perovskite using near-Brewster's angle reflection pump−probe geometry. To acquire the correct dynamical information, the $SCN^-$ anions in the layered perovskite were isotopically diluted, which renders the $^{12}$CN absorption of interest as small as ~2 mOD. In spite of the small optical density, the 2D IR spectra acquired in near-Brewster's angle reflection pump−probe geometry yielded the good-quality data shown in Figure 4. The data reveal the existence of fast structural fluctuations (~4 ps) of the layered perovskite. The nature of the rapid structural changes is schematically illustrated in Figure 4C. The 2D IR observation of spectral diffusion and inhomogeneous broadening of the CN stretch absorption spectrum demonstrates that the lattice structure is dynamically disordered, and the different instantaneous configurations are sampled by thermal fluctuations (Figure 4C). Spectral diffusion reports on the time-dependent sampling of local structural minima of the energy landscape. The structural evolution may be important for the stabilization of optically generated charge carriers or excitons prior to recombination. The results also showed that the CN vibrations on adjacent $SCN^-$ anions are coupled through transition dipole−transition dipole interactions. Although the inorganic layers are structurally and electronically isolated in typical layered perovskites, here the layers are directly linked through $SCN^-$ vibrations.

2D spectroscopy has been applied to other aspects of perovskites. For example, Thouin and co-workers applied 2D visible spectroscopy to another type of 2D perovskite to reveal high bi-exciton binding energy.[57] Applying 2D IR spectroscopy to perovskites requires a vibrational probe. Bakulin and co-workers obtained transmission 2D IR signals from the N−H bending mode of the organic cations in the 3D perovskite $(CH_3NH_3)PbI_3$, and, based on the polarization-dependent peak volumes, they discussed the rotational dynamics of the organic cations.[12,58] A similar method was recently applied to the CN stretching mode of a cation in formamidinium lead iodide perovskite.[59] These experiments addressed orientational dynamics with 2D IR but not spectral diffusion. These same vibrational modes could potentially be employed to track the evolution of the 2D band shapes (spectral diffusion) using the reflection method employed here. There are also a number of reports that $SCN^-$ anions can be doped to replace a fraction of iodides in $(CH_3NH_3)PbI_3$.[60−62] Such doped perovskites might be suitable for studying common 3D systems.

## ■ ASSOCIATED CONTENT

### Supporting Information

The Supporting Information is available free of charge on the ACS Publications website at DOI: 10.1021/jacs.8b03787.

UV−Vis and PL spectra and PXRD patterns of the Pb-I-SCN layered perovskite and discussion of the thickness of the film (PDF)

## ■ AUTHOR INFORMATION

### Corresponding Author

*fayer@stanford.edu

### ORCID

Jun Nishida: 0000-0001-7834-8179



DOI: 10.1021/jacs.8b03787
J. Am. Chem. Soc. 2018, 140, 9882−9890

Daiki Umeyama: 0000-0003-4773-4020
Hemamala I. Karunadasa: 0000-0003-4949-8068
Michael D. Fayer: 0000-0002-0021-1815

### Present Addresses

[†]J.N.: Department of Physics, Department of Chemistry, and JILA, University of Colorado, Boulder, CO 80309
[‡]D.U.: International Center for Materials Nanoarchitectonics (MANA), National Institute for Materials Science (NIMS), 1-1 Namiki, Tsukuba, Ibaraki 305-0044, Japan

### Author Contributions

[§]J.N. and J.P.B. contributed equally to the work.

### Notes

The authors declare no competing financial interest.

## ■ ACKNOWLEDGMENTS

This material is based upon work and instrumentation supported by the Air Force Office of Scientific Research under AFOSR Award No. FA9550-16-1-0104. Support for J.P.B. was provided by the Division of Chemical Sciences, Geosciences, and Biosciences, Office of Basic Energy Sciences of the U.S. Department of Energy through Grant No. DE-FG03-84ER13251. Work by H.I.K., K.P.L., and D.U. was supported by the NSF CAREER award DMR-1351538. D.U. thanks the Japan Society for the Promotion of Science for a postdoctoral fellowship (JSPS Overseas Research Fellowship).

## ■ REFERENCES

(1) Kojima, A.; Teshima, K.; Shirai, Y.; Miyasaka, T. *J. Am. Chem. Soc.* **2009**, *131*, 6050−6051.
(2) Im, J.-H.; Lee, C.-R.; Lee, J.-W.; Park, S.-W.; Park, N.-G. *Nanoscale* **2011**, *3*, 4088−4093.
(3) Lee, M. M.; Teuscher, J.; Miyasaka, T.; Murakami, T. N.; Snaith, H. J. *Science* **2012**, *338*, 643−647.
(4) Bryant, D.; Aristidou, N.; Pont, S.; Sanchez-Molina, I.; Chotchunangatchaval, T.; Wheeler, S.; Durrant, J. R.; Haque, S. A. *Energy Environ. Sci.* **2016**, *9*, 1655−1660.
(5) Chun-Ren Ke, J.; Walton, A. S.; Lewis, D. J.; Tedstone, A.; O'Brien, P.; Thomas, A. G.; Flavell, W. R. *Chem. Commun.* **2017**, *53*, 5231−5234.
(6) Yang, W. S.; Park, B.-W.; Jung, E. H.; Jeon, N. J.; Kim, Y. C.; Lee, D. U.; Shin, S. S.; Seo, J.; Kim, E. K.; Noh, J. H.; Seok, S. I. *Science* **2017**, *356*, 1376−1379.
(7) Arora, N.; Dar, M. I.; Hinderhofer, A.; Pellet, N.; Schreiber, F.; Zakeeruddin, S. M.; Grätzel, M. *Science* **2017**, *358*, 768−771.
(8) Kitazawa, N. *Mater. Sci. Eng., B* **1997**, *49*, 233−238.
(9) Dohner, E. R.; Jaffe, A.; Bradshaw, L. R.; Karunadasa, H. I. *J. Am. Chem. Soc.* **2014**, *136*, 13154−13157.
(10) Poglitsch, A.; Weber, D. *J. Chem. Phys.* **1987**, *87*, 6373−6378.
(11) Yaffe, O.; Guo, Y.; Tan, L. Z.; Egger, D. A.; Hull, T.; Stoumpos, C. C.; Zheng, F.; Heinz, T. F.; Kronik, L.; Kanatzidis, M. G.; et al. *Phys. Rev. Lett.* **2017**, *118*, 136001.
(12) Bakulin, A. A.; Selig, O.; Bakker, H. J.; Rezus, Y. L.; Müller, C.; Glaser, T.; Lovrincic, R.; Sun, Z.; Chen, Z.; Walsh, A.; et al. *J. Phys. Chem. Lett.* **2015**, *6*, 3663−3669.
(13) Wu, X.; Tan, L. Z.; Shen, X.; Hu, T.; Miyata, K.; Trinh, M. T.; Li, R.; Coffee, R.; Liu, S.; Egger, D. A.; et al. *Sci. Adv.* **2017**, *3*, No. e1602388.
(14) Stranks, S. D.; Eperon, G. E.; Grancini, G.; Menelaou, C.; Alcocer, M. J. P.; Leijtens, T.; Herz, L. M.; Petrozza, A.; Snaith, H. J. *Science* **2013**, *342*, 341−344.
(15) D'Innocenzo, V.; Grancini, G.; Alcocer, M. J. P.; Kandada, A. R. S.; Stranks, S. D.; Lee, M. M.; Lanzani, G.; Snaith, H. J.; Petrozza, A. *Nat. Commun.* **2014**, *5*, 3586.
(16) Collavini, S.; Völker, S. F.; Delgado, J. L. *Angew. Chem. Int. Ed.* **2015**, *54*, 9757−9759.
(17) Jha, A.; Duan, H.-G.; Tiwari, V.; Nayak, P. K.; Snaith, H. J.; Thorwart, M.; Miller, R. J. D. *ACS Photonics* **2018**, *5*, 852−860.
(18) Ziffer, M. E.; Mohammed, J. C.; Ginger, D. S. *ACS Photonics* **2016**, *3*, 1060−1068.
(19) Zhu, H.; Miyata, K.; Fu, Y.; Wang, J.; Joshi, P. P.; Niesner, D.; Williams, K. W.; Jin, S.; Zhu, X.-Y. *Science* **2016**, *353*, 1409−1413.
(20) Zheng, F.; Tan, L. Z.; Liu, S.; Rappe, A. M. *Nano Lett.* **2015**, *15*, 7794−7800.
(21) Muljarov, E.; Tikhodeev, S.; Gippius, N.; Ishihara, T. *Phys. Rev. B* **1995**, *51*, 14370.
(22) Smith, M.; Karunadasa, H. *Acc. Chem. Res.* **2018**, *51*, 619−627.
(23) Miyata, K.; Meggiolaro, D.; Trinh, M. T.; Joshi, P. P.; Mosconi, E.; Jones, S. C.; De Angelis, F.; Zhu, X.-Y. *Sci. Adv.* **2017**, *3*, No. e1701217.
(24) Hamm, P.; Zanni, M. T. *Concepts and Methods of 2D Infrared Spectroscopy*; Cambridge University Press: New York, 2011.
(25) Woutersen, S.; Mu, Y.; Stock, G.; Hamm, P. *Proc. Natl. Acad. Sci. U. S. A.* **2001**, *98*, 11254−11258.
(26) Mukherjee, P.; Kass, I.; Arkin, I. T.; Zanni, M. T. *Proc. Natl. Acad. Sci. U. S. A.* **2006**, *103*, 3528−3533.
(27) Fecko, C.; Eaves, J.; Loparo, J.; Tokmakoff, A.; Geissler, P. *Science* **2003**, *301*, 1698−1702.
(28) Kim, Y. S.; Hochstrasser, R. M. *Proc. Natl. Acad. Sci. U. S. A.* **2005**, *102*, 11185−11190.
(29) Zheng, J. R.; Kwak, K.; Asbury, J.; Chen, X.; Piletic, I. R.; Fayer, M. D. *Science* **2005**, *309*, 1338−1343.
(30) King, J. T.; Kubarych, K. J. *J. Am. Chem. Soc.* **2012**, *134*, 18705−18712.
(31) Asbury, J. B.; Steinel, T.; Stromberg, C.; Corcelli, S. A.; Lawrence, C. P.; Skinner, J. L.; Fayer, M. D. *J. Phys. Chem. A* **2004**, *108*, 1107−1119.
(32) Park, S.; Kwak, K.; Fayer, M. D. *Laser Phys. Lett.* **2007**, *4*, 704−718.
(33) Kwak, K.; Park, S.; Finkelstein, I. J.; Fayer, M. D. *J. Chem. Phys.* **2007**, *127*, 124503.
(34) Daub, M.; Hillebrecht, H. *Angew. Chem. Int. Ed.* **2015**, *54*, 11016−11017.
(35) Umeyama, D.; Lin, Y.; Karunadasa, H. I. *Chem. Mater.* **2016**, *28*, 3241−3244.
(36) Xiao, Z.; Meng, W.; Saparov, B.; Duan, H.-S.; Wang, C.; Feng, C.; Liao, W.; Ke, W.; Zhao, D.; Wang, J.; et al. *J. Phys. Chem. Lett.* **2016**, *7*, 1213−1218.
(37) Jaffe, A.; Lin, Y.; Karunadasa, H. I. *ACS Energy Lett.* **2017**, *2*, 1549−1555.
(38) Im, J.-H.; Jang, I.-H.; Pellet, N.; Grätzel, M.; Park, N.-G. *Nat. Nanotechnol.* **2014**, *9*, 927−932.
(39) Nishida, J.; Yan, C.; Fayer, M. D. *J. Chem. Phys.* **2017**, *146*, 094201.
(40) Shim, S.-H.; Zanni, M. T. *Phys. Chem. Chem. Phys.* **2009**, *11*, 748−761.
(41) Kumar, S. K. K.; Tamimi, A.; Fayer, M. D. *J. Chem. Phys.* **2012**, *137*, 184201.
(42) Yan, C.; Thomaz, J. E.; Wang, Y.-L.; Nishida, J.; Yuan, R.; Breen, J. P.; Fayer, M. D. *J. Am. Chem. Soc.* **2017**, *139*, 16518−16527.
(43) Ren, Z.; Brinzer, T.; Dutta, S.; Garrett-Roe, S. *J. Phys. Chem. B* **2015**, *119*, 4699−4712.
(44) Sokolowsky, K. P.; Fayer, M. D. *J. Phys. Chem. B* **2013**, *117*, 15060−15071.
(45) Nishida, J.; Tamimi, A.; Fei, H.; Pullen, S.; Ott, S.; Cohen, S. M.; Fayer, M. D. *Proc. Natl. Acad. Sci. U. S. A.* **2014**, *111*, 18442−18447.
(46) Rosenfeld, D. E.; Gengeliczki, Z.; Smith, B. J.; Stack, T. D. P.; Fayer, M. D. *Science* **2011**, *334*, 634−639.
(47) Giammanco, C. H.; Kramer, P. L.; Yamada, S. A.; Nishida, J.; Tamimi, A.; Fayer, M. D. *J. Phys. Chem. B* **2016**, *120*, 549−556.
(48) Marroux, H. J.; Orr-Ewing, A. J. *J. Phys. Chem. B* **2016**, *120*, 4125−4130.
(49) Yan, S.; Seidel, M. T.; Tan, H.-S. *Chem. Phys. Lett.* **2011**, *517*, 36−40.


DOI: 10.1021/jacs.8b03787
*J. Am. Chem. Soc.* 2018, 140, 9882−9890

(50) Herzberg, G. *Molecular Spectra and Molecular Structure*; Read Books Ltd, 2013; Vol. *1*.
(51) Wong, D. B.; Giammanco, C. H.; Fenn, E. E.; Fayer, M. D. *J. Phys. Chem. B* **2013**, *117*, 623−635.
(52) Golonzka, O.; Khalil, M.; Demirdöven, N.; Tokmakoff, A. *Phys. Rev. Lett.* **2001**, *86*, 2154.
(53) Bian, H.; Wen, X.; Li, J.; Zheng, J. *J. Chem. Phys.* **2010**, *133*, 034505.
(54) Eigner, A. A.; Konold, P. E.; Massari, A. M. *J. Phys. Chem. B* **2009**, *113*, 14549−14554.
(55) Tokmakoff, A. *J. Chem. Phys.* **1996**, *105*, 1−12.
(56) Kwak, K.; Rosenfeld, D. E.; Fayer, M. D. *J. Chem. Phys.* **2008**, *128*, 204505.
(57) Thouin, F.; Neutzner, S.; Cortecchia, D.; Dragomir, V. A.; Soci, C.; Salim, T.; Lam, Y. M.; Leonelli, R.; Petrozza, A.; Kandada, A. R. S.; Silva, C. *Phys. Rev. Mater.* **2018**, *2*, 034001.
(58) Selig, O.; Sadhanala, A.; Muller, C.; Lovrincic, R.; Chen, Z.; Rezus, Y. L.; Frost, J. M.; Jansen, T. L.; Bakulin, A. A. *J. Am. Chem. Soc.* **2017**, *139*, 4068−4074.
(59) Taylor, V. C. A.; Tiwari, D.; Duchi, M.; Donaldson, P. M.; Clark, I. P.; Fermin, D. J.; Oliver, T. A. A. *J. Phys. Chem. Lett.* **2018**, *9*, 895−901.
(60) Tai, Q.; You, P.; Sang, H.; Liu, Z.; Hu, C.; Chan, H. L.; Yan, F. *Nat. Commun.* **2016**, *7*, 11105.
(61) Halder, A.; Chulliyil, R.; Subbiah, A. S.; Khan, T.; Chattoraj, S.; Chowdhury, A.; Sarkar, S. K. *J. Phys. Chem. Lett.* **2015**, *6*, 3483−3489.
(62) Chen, Y.; Li, B.; Huang, W.; Gao, D.; Liang, Z. *Chem. Commun.* **2015**, *51*, 11997−11999.


DOI: 10.1021/jacs.8b03787
*J. Am. Chem. Soc.* 2018, 140, 9882−9890